AIP | Journal of Applied Physics

Functional gradation through preferential crystallisation and interfacial activity in rapidly quenched Fe/Co-based bilayered ribbons for bend sensors

A. K. Panda, R. K. Roy, Sushmita Dey, Satnam Singh, and A. Mitra

Citation: J. Appl. Phys. **114**, 023909 (2013); doi: 10.1063/1.4813222
View online: http://dx.doi.org/10.1063/1.4813222
View Table of Contents: http://jap.aip.org/resource/1/JAPIAU/v114/i2
Published by the AIP Publishing LLC.

JOURNAL OF APPLIED PHYSICS **114**, 023909 (2013)

Functional gradation through preferential crystallisation and interfacial activity in rapidly quenched Fe/Co-based bilayered ribbons for bend sensors

A. K. Panda,[a] R. K. Roy, Sushmita Dey, Satnam Singh, and A. Mitra
NDE & Magnetic Materials Group, Material Science & Technology Division, CSIR-National Metallurgical Laboratory, Jamshedpur 831007, India

(Received 22 April 2013; accepted 20 June 2013; published online 12 July 2013)

Rapidly quenched bilayered ribbons comprising one layer as $Fe_{73.5}Nb_3Cu_1Si_{13.5}B_9$ (FM) and the other layer either as $Fe_{74.5}Nb_3Si_{13.5}B_9$ (FNb) or $Co_{72.5}Si_{12.5}B_{15}$ (CSB) alloy designated as $BL_{FM/FNb}$ and $BL_{FM/CSB}$, respectively, have been addressed. Phase transformation, thermomagnetic transitions, saturation magnetization, and soft magnetic properties of individual layers were revealed in the functional properties of bilayered ribbons. Properties of bilayer could be endorsed with respect to the single layered $Fe_{73.5}Nb_3Cu_1Si_{13.5}B_9$, $Fe_{74.5}Nb_3Si_{13.5}B_9$, and $Co_{72.5}Si_{12.5}B_{15}$ alloy ribbons. Selective devitrification of the layers in the bilayers could be induced through optimum heat treatment. Enhanced bend sensitivity was revealed in $BL_{FM/CSB}$ through generation of desirable phases in the bilayers of the bilayered ribbon. Synergistic diffusivity of Fe and Co with its consequent effect on interfacial zone of $BL_{FM/CSB}$ bilayer was observed. © *2013 AIP Publishing LLC*. [http://dx.doi.org/10.1063/1.4813222]

I. INTRODUCTION

The synergy between micro-mechanics and sensitivity of functional materials is of paramount significance for enhancing sensor efficiency. In recent years, these materials have occupied important segments of sensors and actuators. Amongst such materials, rapidly quenched ribbons have been explored as stress, torque,[1] magnetic shape memory,[2] and thermal sensors.[3] Subsequently, it was found that nanocrystallisation of soft magnetic glassy precursors is a potential microstructural evolution methodology for improving the properties of materials to develop sensors. In these cases, nanostructured phases in metallic composites change the magnetostriction (λ_S) of the system which consequently modifies the functional properties. In the Fe-based alloy, the critical balance between positively magnetostrictive ($+\lambda_S$) glassy matrix and negatively magnetostrictive ($-\lambda_S$) of FeSi-nanophase led to reduction in "λ_S" of the material.[4] This resulted into enhancement in the soft magnetic properties like low coercivity and high permeability. Such enhanced properties are also observed in $+\lambda_S$ and $-\lambda_S$ magnetostrictive materials when subjected to tensile and compressive stresses, respectively. During bending, the upper and lower portions of the materials experience two opposing types of stresses, wherein the top layer is in tensile while bottom layer is in compressive state. Thus, in a single layer (SL) ribbon, the contribution towards by stress in one surface of ribbon is nullified by the other. Such deleterious effects of the counter surface open the scope of development of bilayered (BL) materials with different functional properties.[5]

In the quest to develop functionally graded bilayers materials, bend sensors have been explored using ribbons agglutinated to counter non-magnetic metallic base.[6] Agglutination of a metallic ribbon to either another metallic ribbon or a counter polymer ribbon lowers the sensor output due to thickness of the glue. Welding of layers has a tendency of generating inhomogeneous force distribution between the two bilayers. Thus, attempts have been made to develop monolithic bilayers of Fe6.5Si/FeMnCrSiB and Fe-based amorphous/nanocrystalline ribbons, wherein the investigation has been limited only to their magnetic response.[7,8] In the application arena, rapidly quenched metastable metallic ribbon, layered on a polymer or nonmetallic base, has been observed for biomedical applications like monitoring chest wall displacements (cardio-respiratory activity).[9] Static curvatures (airplane wings, optical lenses)[10] and dynamic measurements like airflow detectors[11] have also been investigated. The potential property of magnetostriction in biosensor platforms comprising amorphous magnetostrictive $Fe_{80}B_{20}$ layer coated with a biomaterial has also been reported recently.[12]

Despite exploration of bilayered systems with combination of a magnetic ribbon with a counter magnetic or non-magnetic base, proper choice of glassy systems which can contribute towards selective structural modifications and effective functional gradation is under investigation. The present study is focussed on a controlled crystallisation and its effect on the structural, magnetic, and bend sensitivity of two sets of bilayered ribbons with one set as $Fe_{73.5}Nb_3Cu_1Si_{13.5}B_9/Fe_{74.5}Nb_3Si_{13.5}B_9$ and another one in the form of $Fe_{73.5}Nb_3Cu_1Si_{13.5}B_9/Co_{72.5}Si_{12.5}B_{15}$ bilayer.

II. MATERIAL PREPARATION

Alloys $Fe_{73.5}Nb_3Cu_1Si_{13.5}B_9$ (FM), $Fe_{74.5}Nb_3Si_{13.5}B_9$ (FNb), and $Co_{72.5}Si_{12.5}B_{15}$ (CSB) were melt spun into single layered ribbons designated as SL_{FM}, SL_{FNb}, and SL_{CSB}, respectively. Two different BL ribbons $BL_{FM/FNb}$ and $BL_{FM/CSB}$ were also prepared by using double nozzle technique (DNT).[13] In this process, two different alloys were taken in the dual chambers of a quartz crucible, induction melted and ejected simultaneously through the double nozzles on a rotating Cu-wheel. The orientation of the crucible nozzles was

[a]Electronic addresses: akpanda@nmlindia.org and akpanda2_in@rediffmail.com. Tel.: +91-657-2345002. Fax: +91-657-2345213.

maintained in such a way so that the FM formed the top layer while FNb and CSB are the bottom layers of $BL_{FM/FNb}$ and $BL_{FM/CSB}$ bilayers, respectively.

III. EXPERIMENTAL

Magnetostriction (λ_S) of the ribbons was measured using a parallel plate capacitance based device developed in the laboratory. The thermal and structural properties were evaluated by a Differential scanning calorimeter (Perkin Elmer Diamond DSC) and an x-ray diffractometer (XRD), respectively. The diffractometer has a Cu-Kα target. Magnetisation studies at room and at elevated temperatures were carried out using a Vibrating sample magnetometer (Lakeshore VSM 7404) with furnace attachment. The coercivity was measured using a B-H loop tracer. The elemental distribution across bilayer cross-section was observed using an electron probe microanalyser (EPMA: JXA-8230, JEOL). The bending sensitivity of the ribbons was determined using a setup developed in the laboratory, the scheme of which is shown in Fig. 1. The ribbon is placed within the polymer channel guide, which extended equally on either side across the hinge. A magnetising voltage of 500 mV at a frequency of 100 kHz was applied through a magnetising coil which also serves as the pick-up coil. The free aluminium platform with a friction controlled hinge is bent to desired angle "θ" and the inductance value is measured using an impedance analyser (Agilent 4294A). As the ribbons are sensitive to stress, bending induces change in permeability of the ribbons via self induction "S_L," resulting into proportional change in permeability. For this measurement, a non-contact magnetic flux pick-up coil has been reported[5] to sense the inductive voltage "v" given by the relation

$$(v) = -Ns\frac{d\phi}{dt}, \tag{1}$$

$$\text{Since, } \phi \propto f(\mu, \delta, i), \tag{2}$$

$$(v) = -Ns\frac{d\phi(\mu, \delta, i)}{dt}, \tag{3}$$

where "N_S" is number of turns in pick-up coil, "μ" is permeability, "δ" is distance of pick-up coil from sensor element, and "i" is magnetising current. In the present device, "N_S" and "i" are constant while "δ" function is neglected due to the coil encircling the sensor element. Thus, Eq. (1) modifies with the incorporation of constant "k" for magnetising current per unit turns and can be written as

$$S_L = v = -k'\frac{d\phi(\mu)}{dt}. \tag{4}$$

In the present setup when the ribbon is bent, the curvature near the flange induces stress effects on the ribbon. This local stress causes relative change in the permeability. As a result, the secondary induced voltage in the magnetising coil changes which is measured in terms of inductance using an impedance analyser.

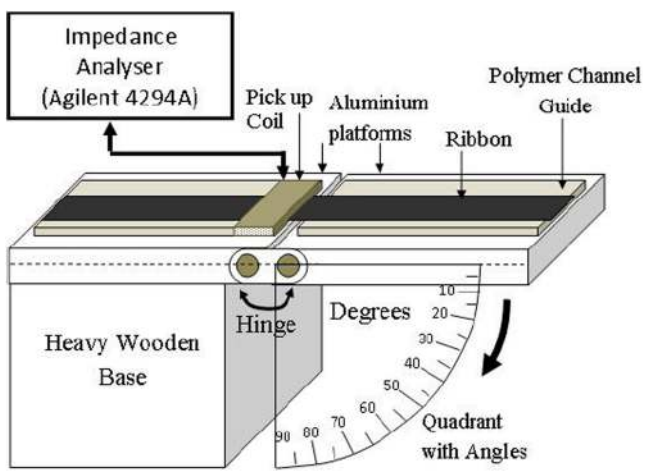

FIG. 1. Schematic presentation of the bending device.

IV. RESULTS AND DISCUSSION

The structure of as-spun bilayered ribbons at its top and bottom layers separately was observed using an x-ray diffractometer. The bilayered ribbons, $BL_{FM/FNb}$ and $BL_{FM/CSB}$, reveal their amorphous state with a broad diffraction peak maxima (Fig. 2(a)). The diffractograms of separate layers have been shown in the inset of Fig. 2(a). DSC plots reveal that bilayered $BL_{FM/FNb}$ and $BL_{FM/CSB}$ ribbon undergo exothermic transformation (Fig. 3) with distinct onsets of crystallisation (Table I). It is observed that crystallisation onsets of single layered ribbons are manifested characteristically in the bilayered ribbons as indicated by arrows in the table. The primary crystallisation onset "T_{X1}" for SL_{FM} at 528 °C is revealed as onsets of transformation at 534 °C and 532 °C in $BL_{FM/FNb}$ and $BL_{FM/CSB}$, respectively. Similarly, primary crystallisation stage "T_{X2}" at 595 °C for SL_{FNb} and 567 °C for SL_{CSB} appear at 600 °C and 567 °C in their corresponding bilayers. The secondary (T_{X2} = 585 °C) and tertiary (T_{X3} = 567 °C) crystallisation stages of SL_{CSB} emerge at similar onsets in the bilayer $BL_{FM/CSB}$.

To analyse the phases generated when approaching primary crystallisation onset, x-ray diffractograms (Fig. 2(b)) were obtained for the bilayered ribbons annealed at 500 °C. It is found that the FM-layer indicated incipient crystallisation of α-FeSi/F_3Si (space group Im3m) phase with a relatively sharper x-ray diffraction peak as compared to higher crystallisation onset of FNb- and CSB-layers. From the principle of full width at half maxima (FWHM), the particle size of α-FeSi/F_3Si in SL_{FM} was found to be ~6–7 nm using Debye Scherrer equation. The particle size in FM-alloy is low in comparison with the reported values of 12–15 nm.[14] This low value is expected due to its low annealing temperature (500 °C) as compared to its crystallisation onsets in the range of 528 °C to 534 °C observed in the single and bilayer. The SL_{FNb} shows broader x-ray diffractogram indicating its vitrified state, though nanoscale incipient segregation is not ruled out. The SL_{CSB} indicates diffraction peaks of hcp-Co phase. This phase may be in small volume fraction (low intensity primary and higher order reflections)[15] in view of its far lower annealing temperature (500 °C) compared to crystallisation onsets of 567 °C (Fig. 3).

The evolution of the phases also influences the thermal stability and magnetic moment of these alloys in the bilayers,

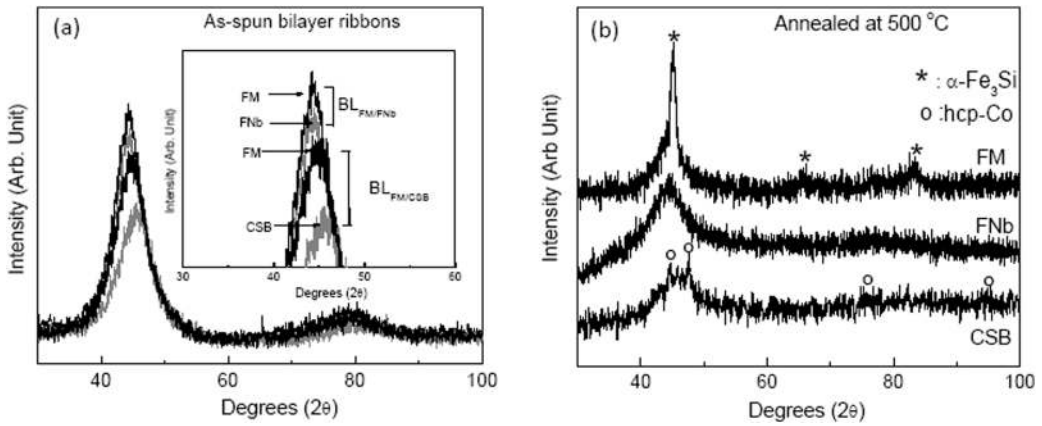

FIG. 2. X-ray diffractograms of (a) as-spun ribbons and (b) ribbons annealed at 500 °C.

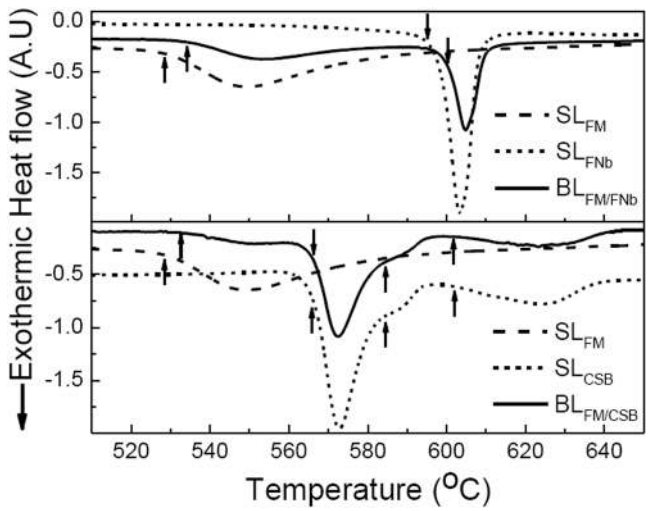

FIG. 3. DSC plots of SL and BL as-quenched ribbons.

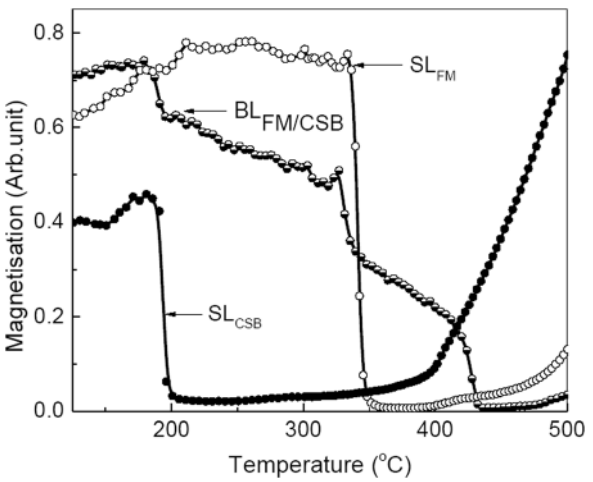

FIG. 4. Thermomagnetic plots single layered (SL_{FM}, SL_{CSB}) and bilayered ($BL_{FM/CSB}$) as-quenched ribbons.

which is revealed from their thermomagnetic transition temperatures (Fig. 4) and indicated in Table II. The ferromagnetic to paramagnetic transitions (inset of Fig. 4) of amorphous matrix indicates its (T_{C1}) occurring at 190 °C and 342 °C SL_{FM} and for SL_{CSB}, respectively. These transitions appear as step-drops at 190 °C (T_{C1}) and 332 °C (T_{C2}) in the magnetisation profile of $BL_{FM/CSB}$. The first transition is not complete due to high magnetic moment of FM layer, while the second transition is counter balanced by formation of hcp-Co in the CSB layer. In the case of SL_{CSB}, the gradual rise in magnetisation beyond 250 °C is attributed to incipient segregation of hcp-Co which is also evidenced by small peak intensities in x-ray diffractogram (Fig. 2(b)) of SL_{CSB} annealed at 500 °C. Such segregates occur prior to silicide formation at 567 °C (T_{X1}). In $BL_{FM/CSB}$, the drop in magnetisation at 435 °C (T_{C3}) indicates the Curie temperature of the FM layer, which is shifted to such high temperature due to

TABLE I. DSC crystallisation onsets of single layered and bilayered ribbons.

Single Layered / Bilayered Ribbons	Crystallization Temperature (°C)			
	T_{X1}	T_{X2}	T_{X3}	T_{X4}
SL_{FM}	528	-	-	-
SL_{FNb}	595	-	-	-
$BL_{FM/FNb}$	534	600	-	-
SL_{CSB}	567	585	602	
$BL_{FM/CSB}$	532	567	585	602

TABLE II. Ferromagnetic ordering temperatures obtained from thermomagnetic plots.

Single Layered / Bilayered Ribbons	Curie Temperature (°C)		
	T_{C1}	T_{C2}	T_{C3}
SL_{FM}	342	-	-
SL_{FNb}	350	-	-
$BL_{FM/FNb}$	350	-	-
SL_{CSB}	190	-	-
$BL_{FM/CSB}$	190	332	435

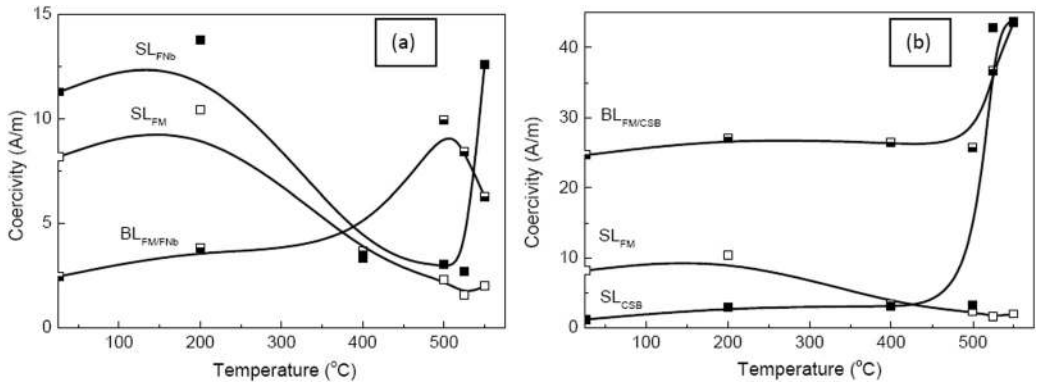

FIG. 5. Thermal variation of coercivity in (a) $BL_{FM/FNb}$ and (b) $BL_{FM/CSB}$ along with their single layered ribbons.

drastic rise in magnetisation of FM and CSB layer. In the case of $BL_{FM/FNb}$, thermomagnetic transition T_{C1} is equal to that of SL_{FNb} and closer to that of SL_{FM}. At temperatures closer to 500 °C, the SL_{FM} ribbon showed rise in magnetisation due to the formation of α-Fe_3Si phase (Fig. 2(b)) with higher magnetic moment.

Thermal response of coercivity (Fig. 5) also throws light on the contribution of FM layer on the crystallisation and magnetic transitions of the bilayer. The FM layer (Fig. 5(a)) in $BL_{FM/FNb}$ counteracts the rapid deterioration in soft magnetic property (coercivity increase) and compensates for detrimental profile beyond 500 °C occurring due to the FNb-layer. This is attributed to by far a controlled phase transformation exhibited by a shallow DSC exotherm[16] of "FM" alloy showing nanocrystallisation in this layer. The presence of Cu in this layer facilitates heterogeneous nanophase formation along with grain growth impeding element Nb which slows down the kinetics of transformation.[17] This gives the advantage of averaged anisotropy of nanoparticles based on Herzer's random anisotropy model (RAM).[18] However, the phenomenon of drastic deterioration contributed by the CSB layer (Fig. 5(b)) in the span of 400 °C to 500 °C cannot be compensated by the FM layer and hence the bilayer $BL_{FM/CSB}$ also follows the deteriorating trend beyond 500 °C. The highly anisotropic nature of clusters of hcp-Co sets in deterioration of soft magnetic properties prior to primary crystallisation onset.[19] To understand the effect of functionalisation, thermal variation of coercivity has been analysed with respect to the initial as-quenched state. In this analysis, coercivity values of combining single layered ribbons are averaged and then the averaged data are normalised with respect to averaged as-quenched values. Similarly, the bilayered coercivity data are normalised with the as-quenched values. The plot profiles of the normalised values are shown in Fig. 6. Although the bilayer $BL_{FM/FNb}$ showed a magnetic hardening effect up to 500 °C compared to the averaged value of its single layers, the influence of nanocrystallisation due to FM layer has a dominating effect in improving the property of the bilayer. Similarly, the functional effect of magnetic enhancement was also evidenced in the bilayer $BL_{FM/CSB}$ with its slower kinetics of deterioration with elevation in temperature. The influence of individual alloy layers is also observed in the saturation magnetisation values (M_S) of the bilayers (Fig. 7). The M_S values of the bilayer $BL_{FM/CSB}$ lie between those of single layered ribbons SL_{FM} and SL_{CSB}. However, the $BL_{FM/FNb}$ has values much closer to those of SL_{FNb} as the difference in saturation magnetisation values of SL_{FM} and SL_{FNB} is very small.

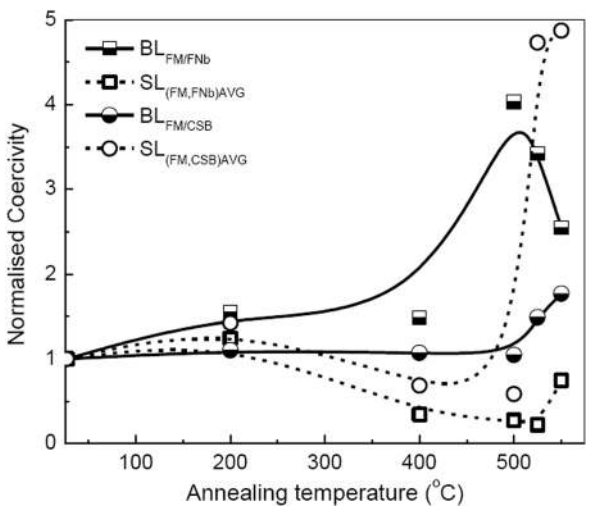

FIG. 6. Variation of coercivity with annealing temperature in bilayered ribbons and averaged coercivity of single layered ribbons.

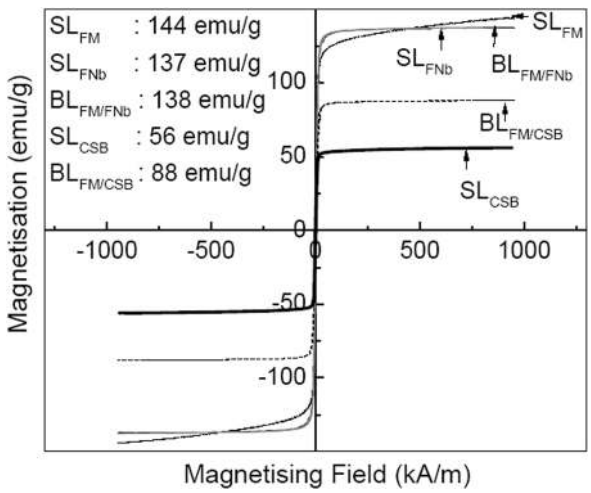

FIG. 7. Magnetisation plots of single and bilayered as-spun ribbons.

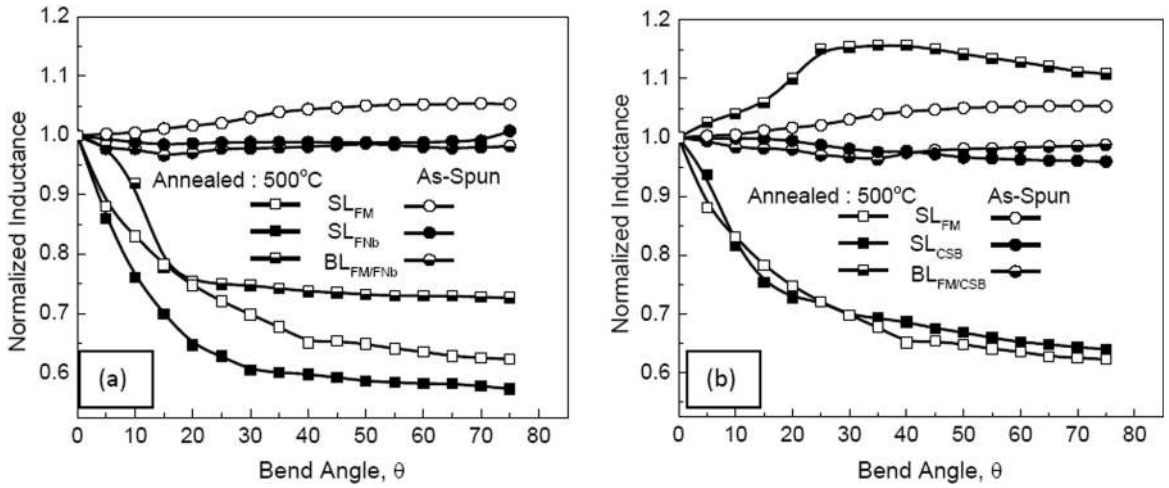

FIG. 8. Bend sensitivity of bilayers (a) $BL_{FM/FNb}$, (b) $BL_{FM/CSB}$ and their respective single layered as-spun ribbons.

The bending sensitivity can be explained on the basis of magnetostriction, stress state, and structural developments. The pre-stress (bend) values are initially deducted from the inductance values "S_L" obtained in Eq. (4) and then normalised with respect to the zero bend state. The variation of the inductance with bend angle is shown for $BL_{FM/FNb}$ and $BL_{FM/CSB}$ bilayered ribbons along with their corresponding single layer ribbons in Figs. 8(a) and 8(b), respectively. The inductance data for corresponding single layers are also shown in the plots. In as-spun state, the bend sensitivity of SL_{FNb} and $BL_{FM/FNb}$ is comparable (Fig. 8(a)). Sensitivity towards bend is observed in the case of as-spun SL_{CSB} and $BL_{FM/CSB}$ (Fig. 8(b)). In both the cases, the single layer ribbon SL_{FM} indicates higher sensitivity with increasing bend angle. The influence of structural developments as a functional gradation of magnetostriction and consequent effect on bending stress is schematically presented in Fig. 9. To further explain the bend sensitivity, magnetostriction of SL_{FM}, SL_{FNb}, and SL_{CSB} was measured. SL_{FM} indicated higher bend sensitivity due to its higher positive λ_S (Fig. 10). In the case of bilayer $BL_{FM/FNb}$, the bottom FNb layer with small positive ($\lambda_S > 0$) magnetostriction results in the compressive stress (σ_{CS}) which counteracts the rise in inductance due to tensile stress (σ_{TS}) generated at the top FM layer. Thus, the overall bend sensitivity does not enhance the bilayer $BL_{FM/FNb}$ with bend angle. Similarly, the as-spun $BL_{FM/CSB}$ does not indicate any enhancement in bend sensitivity due to the fact that in bottom CSB-layer, the negative λ_S ($\lambda_S < 0$) is small enough to enhance the overall inductance of the bilayer subjected to bending. Upon annealing at 500 °C, the incipient generation of negatively magnetostrictive ($-\lambda_S$) α-FeSi/F_3Si (space group Im3m) dispersed in FeNbB amorphous matrix (precursor metastable state) with +ve λ_S reduces the overall magnetostriction in FM layer.[20] Thus, the bend sensitivity of $BL_{FM/FNb}$ annealed at 500 °C is reduced as compared to as-spun state. However, in SL_{FNb},

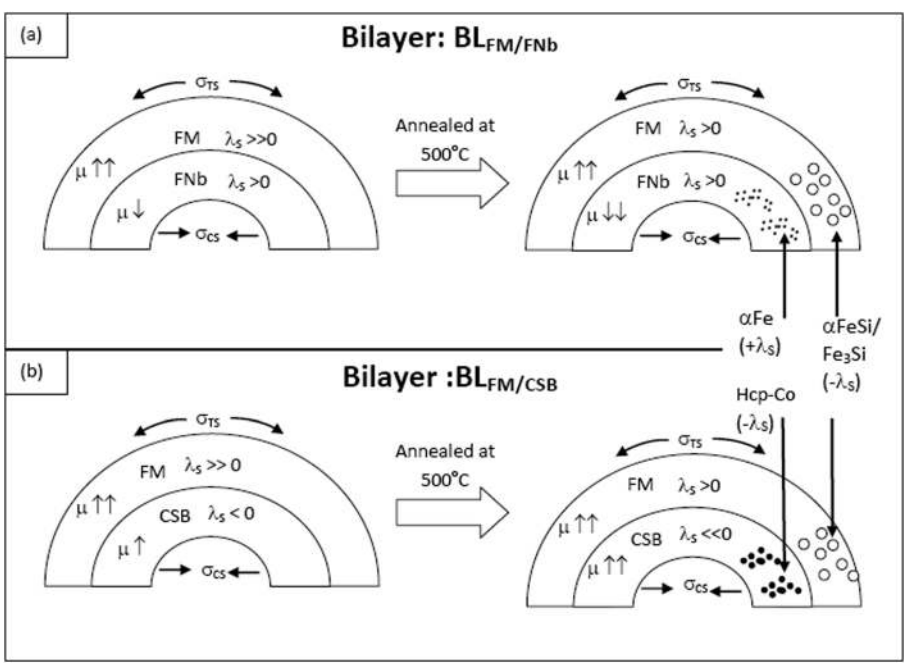

FIG. 9. Scheme showing mechanism of selective structural modifications on magnetostriction (λ_S) and permeability (μ) wherein arrows (↑) and (↓) indicated rise or drop, respectively, in the as-spun and heat treated bilayers (a) $BL_{FM/FNB}$ and (b) $BL_{FM/CSB}$ ribbons. αFe, Hcp-Co segregations are representative.

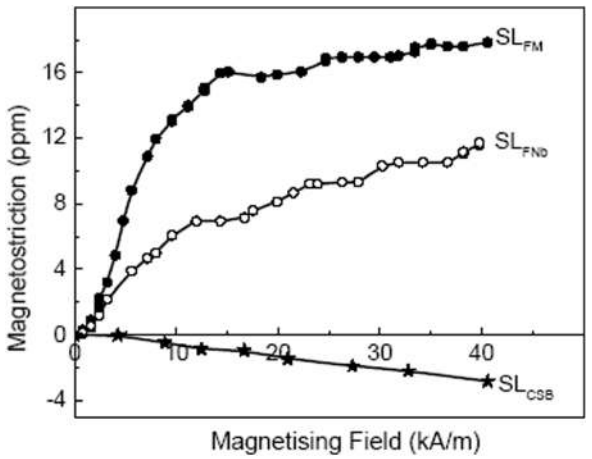

FIG. 10. Variation of magnetostriction with applied magnetic field in SL_{FM}, SL_{FNb}, and SL_{CSB} ribbons.

the generation of α-Fe ($+\lambda_S$) reduces the inductance in the "σ_{CS}" state and thus lowers the bend sensitivity compared to its as-spun state. The combined effect of SL_{FM} and SL_{FNb} in bilayer reduced its bend sensitivity on annealing at 500 °C. In the case of $BL_{FM/CSB}$, the generation of hcp-Co in CSB-layer further enhanced the permeability and thus the inductance in the compressive bottom layer. The generation of hcp-Co further lowered the λ_S of CSB-layer which improved the permeability in the compressive state "σ_{CS}" of the bottom layer of $BL_{FM/CSB}$. Thus, in $BL_{FM/CSB}$, the bend sensitivity increased with increasing bend angle. The generation of α-Fe and hcp-Co in the bottom layers "FNb" and "CSB," respectively, have indicated their signatures in the EPMA elemental profile shown in Fig. 11. The $BL_{FM/FNb}$ indicated the drop in Fe concentration as the profile proceeds from FM to FNb layers of this bilayer. The phenomenon of diffusion and generation of interfacial layers in the nano-regime is schematically presented in Fig. 12. The interdiffusion of Fe across the interface results in fluctuation in the concentration. Similar fluctuation in Fe and Co content is also observed across $BL_{FM/CSB}$. Elemental line profile analysis shows the depletion zones of the Fe concentration denoted as $Fe_{FM\text{-}DZ}$ and $Fe_{FNb\text{-}DZ}$ ~1.4 μm each and close to the interface diffusing zone (D_{FZ}) layer ~1.42 μm. The profile of Fe indicates diffusion of the Fe atoms leading to a rise in its concentration which is more or less symmetric across the zone. This is due to the near equal compositional stoichiometry of Fe in "FM" and "FNb" layers on either side of the bilayer $BL_{FM/FNb}$. Elemental profiles of Fe and Co indicate similar depletion zones $Fe_{FM\text{-}DZ}$ and $Co_{CSB\text{-}DZ}$ in the bilayer $BL_{FM/CSB}$. Interestingly, the Fe and Co diffusions indicate a non-symmetric concentration profiles at the interface. The synergistic variation of Fe (increase/decrease) and Co (decrease/increase) concentration is clearly evidenced in Fig. 11 and represented in the scheme of Fig. 12. This is suggestive of the fact that these two elements are miscible along a wide range of their compositions and lowers their interfacial energy.[21] The diffusion zone "D_{FZ}" ~ 0.6 μm evolving a synergistic change in Fe-Co concentration indicates a revealing demarcation zone between the two layers of the bilayer $BL_{FM/CSB}$. The EPMA image indicates the visible demarcation interface in $BL_{FM/CSB}$ as compared to a more diffused

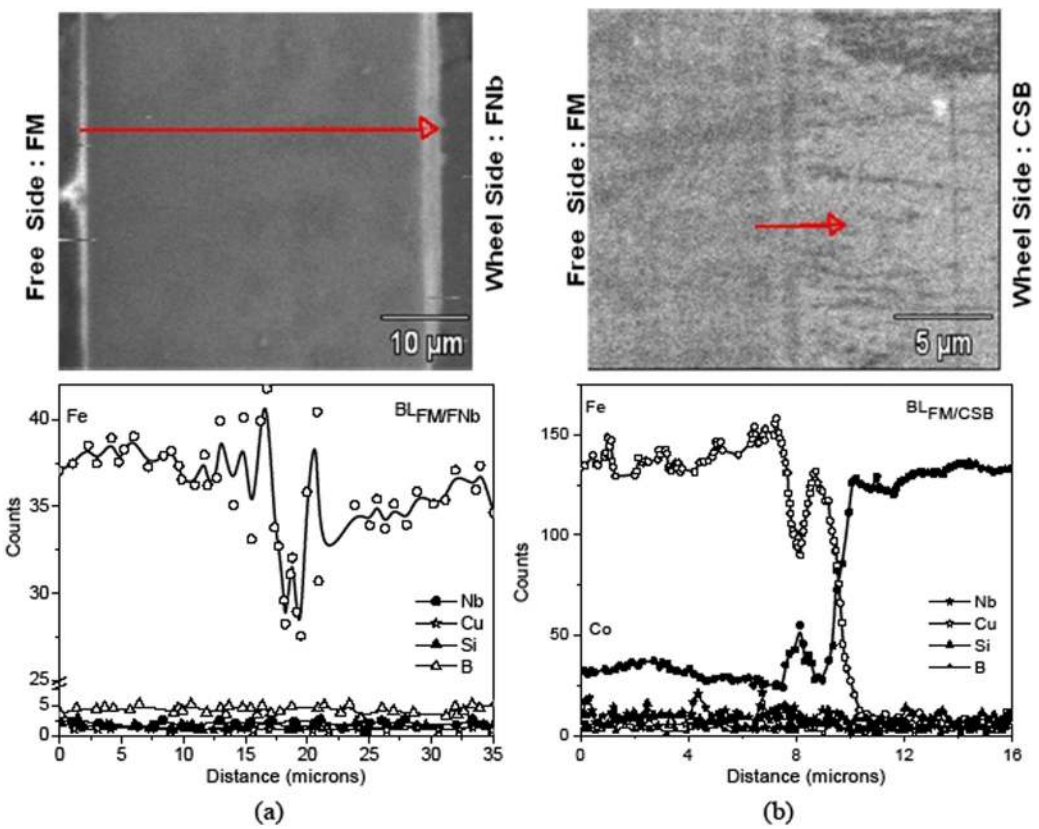

FIG. 11. EPMA micrographs and elemental distribution of bilayers (a) $BL_{FM/FNb}$, (b) $BL_{FM/CSB}$ ribbons.

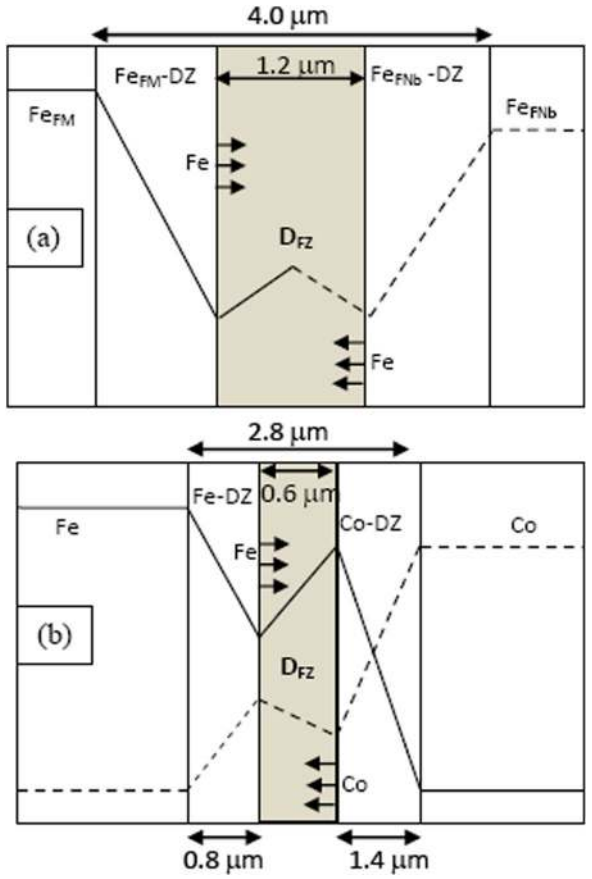

FIG. 12. Schematic presentation of the EPMA elemental line profiles of (a) $BL_{FM/FNb}$ and (b) $BL_{FM/CSB}$ bilayers showing interface layers and elemental diffusion (arrows).

one in $BL_{FM/FeNb}$. Such distinct interfacial layer due to interdiffusion of Co and Fe in $SmCo_5$/Fe and Sm_2Co_7/Fe/Sm_2Co_7 thin films have also been reported.[22] In the bilayer $BL_{FM/CSB}$, the drop in the concentration of Fe is followed by a drastic rise in the gradient of Fe in the diffusivity zone "D_{FZ}" and the corresponding gradient of Co diffusivity profile is alternatively varied in the "D_{FZ}" zone. The diffusivity of either Fe or Co as tracer element into the Co-based and Fe-based layer, respectively, has been estimated using intrinsic diffusivity equation

$$D = Ae^{(-Q/RT)}, \tag{5}$$

$$\text{or} \quad \log D = \log A - \frac{Q}{2.303R}\left(\frac{1}{T}\right), \tag{6}$$

where A is the frequency factor, i.e., maximum diffusion coefficient at infinite temperature, Q is activation energy, R is gas constant, and T is the temperature of diffusion. T is the melt ejection temperature and which is also assumed to be the temperature of diffusion in the case of rapid solidification processing through melt spinning. The calculated diffusivity coefficient from the standard diffusivity parameters of the tracer elements[23] are shown in Table III. From Eq. (6), coefficients D_{Co}^{Fe} and D_{Fe}^{Co} have the values of 4.72×10^{-14} m^2/s and 1.06×10^{-14} m^2/s, respectively. The higher values of D_{Co}^{Fe} is attributed to sharper and higher diffusivity gradient as compared to D_{Fe}^{Co} in the bilayer $BL_{FM/CSB}$. Analysing the present result, it is suggested that due to such a phenomenon occurring in $SmCo_5$ thin film, the FeCo layer has been found to be thicker in the Fe-rich zone of the thin film.[23] In the present investigation, the diffusivity is also supposed to continue for some time even beyond the melt solidification front as long as the ribbon has the critical temperature for diffusivity. The compositional profiles of the rest of the elements Nb, Cu, Si, and B is consistent either due to their low concentrations (Nb, Cu) or due to their near equal content (Si, B) in the individual layers of the bilayers.

TABLE III. Diffusivity coefficients determined for the interface layer using tracer element data and rapid solidification temperature.

Tracer element	Host layer of bilayer	A (m^2/s) (10^{-4})	Q (kJ/mol)	T (K)	Calculated D (m^2/s) (10^{-14})
Fe	CSB	0.11	253.30	1583	4.72 D_{Co}^{Fe}
Co	FM	1.0	301.90	1583	1.06 D_{Fe}^{Co}

V. CONCLUSIONS

The bilayered rapidly quenched amorphous ribbons $BL_{FM/FNb}$ and $BL_{FM/CSB}$ exhibited functional gradation in properties. Crystallisation onsets, saturation magnetisation, and Curie temperature of the single layered ribbons SL_{FM}, SL_{FNb}, and SL_{CSB} are revealed in the bilayered ribbons. A bend sensor based on change in self inductance for ribbon sample was designed. The bend angle sensitivity of $BL_{FM/FNb}$ and $BL_{FM/CSB}$ in annealed ribbons depends on the partial crystallisation of the layers in the bilayered ribbons. The behaviour has been correlated to the structural modification in the individual layers of the bilayers. In the annealed state, the formation of the α-FeSi in "FM" layer and hcp-Co in "CSB" layer of the $BL_{FM/CSB}$ improved the bending sensitivity of the bilayer. This opened the scope of the bilayer as a material for surface profile detectors and bend sensors. In the bilayered ribbon $BL_{FM/CSB}$, the fluctuation in the concentration of iron and cobalt at the interface layer is correlated to their diffusivity coefficients and concentration gradient.

ACKNOWLEDGMENTS

The authors express their sincere gratitude to Director, CSIR-National Metallurgical Laboratory (CSIR-N.M.L), Jamshedpur, India, for his kind permission to carry out and publish the work. One of the authors (A.K.P.) acknowledges Dr. Peter Svec and Dr. Dusan Janickovic, Slovak Academy of Sciences for the experience gained on bilayered ribbons during his visit to the Academy under INSA visiting program.

[1]I. Giouroudi, J. Kosel, H. Pfutzner, and W. Brenner, Sens. Actuators, A **142**, 474 (2008).
[2]S. Singh, R. K. Roy, M. Ghosh, A. Mitra, and A. K. Panda, J. Appl. Phys. **112**, 103512 (2012).
[3]E. Kaniusas, L. Mehnen, and H. Pfutzner, J. Magn. Magn. Mater. **254–255**, 624 (2003).
[4]M. E. McHenry, M. A Willard, and D. E. Laughlin, Prog. Mater. Sci. **44**, 291 (1999).

[5]J. Kosel *et al*., Sens. Actuators, A **123–124**, 349 (2005).
[6]L. Mehnen, H. Pfutzner, and E. Kaniusas, J. Magn. Magn. Mater. **215–216**, 779 (2000).
[7]D. Imamura, T. Todaka, and M. Enokizano, IEEE Trans. Mater. **47**, 3184 (2011).
[8]Y. Sato, M. Fujikura, Y. Haga, and T. Sato, J. Magn. Soc. Jpn. **20**, 505 (1996).
[9]E. Kaniusas, L. Mehnen, C. Krell, and H. Pfutzner, J. Magn. Magn. Mater. **215–216**, 776 (2000).
[10]H. Pfutzner *et al*., J. Mater. Process. Technol. **181**, 186 (2007).
[11]G. S. Katranas and T. Meyden, IEEE Trans. Magn. **43**, 2382–2384 (2007).
[12]S. Li, S. Horikawa, M.-K. Park, Y. Chai, V. J. Vodyanoy, and A. B. Chin, Intermetallics **30**, 80 (2012).
[13]L. Mehnen, P. Svec, H. Pfutzner, and P. Duhaj, J. Magn. Magn. Mater. **254–255**, 627 (2003).
[14]M. E. McHenry, F. Johnson, H. Okumura, T. Ohkubo, V. R. V. Ramanan, and D. E. Laughlin, Scr. Mater. **48**, 881 (2003).
[15]P. R. Ohodnicki, Jr., D. E. Laughlin, M. E. McHenry, and M. Widom, Acta Mater. **58**, 4804 (2010).
[16]O. Mohanta, A. Basumallick, A. Mitra, and A. K. Panda, J. Magn. Magn. Mater. **322**, 112 (2010).
[17]Y. Yoshizawa, S. Oguma, and K. Yamauchi, J. Appl. Phys. **64**, 6044 (1988).
[18]G. Herzer, Acta Mater. **61**, 718 (2013).
[19]O. Mohanta, M. Ghosh, A. Mitra, and A. K. Panda, J. Phys. D: Appl. Phys. **42**, 065007 (2009).
[20]G. Vlasak, P. Duhaj, and P. Svec, J. Magn. Magn. Mater. **140–144**, 443 (1995).
[21]P. R. Ohodnicki, Jr., Y. L. Qin, D. E. Laughlin, H. E. McHenry, M. Kodzuka, T. Ohkubo, K. Hono, and M. A. Willard, Acta Mater. **57**, 87 (2009).
[22]Y. Zhang, M. J. Karamer, D. Banerjee, I. Takeuchi, and J. Pinglu, J. Appl. Phys. **110**, 053914 (2011).
[23]*Smithell Metal Reference Book*, 7th ed., edited by E. A. Brandes and G. B. Brook (Butterworth-Heinemann Publications, 1992).